

Article

Crystal Chemistry and Stability of Hydrated Rare-Earth Phosphates Formed at Room Temperature

Asumi Ochiai and Satoshi Utsunomiya *

Department of Chemistry, Kyushu University, 744 Motoooka, Nishi-ku, Fukuoka 819-0395, Japan; a.ochia@chem.kyushu-univ.jp

* Correspondence: utsunomiya.satoshi.998@m.kyushu-u.ac.jp; Tel.: +81-92-802-4168

Academic Editor: Denis Gebauer

Received: 29 April 2017; Accepted: 17 May 2017; Published: 19 May 2017

Abstract: In order to understand the crystal chemical properties of hydrous rare-earth (RE) phosphates, $\text{REPO}_{4,\text{hyd}}$, that form at ambient temperature, we have synthesized $\text{REPO}_{4,\text{hyd}}$ through the interaction of aqueous RE elements (REEs) with aqueous P at room temperature at $\text{pH} < 6$, where the precipitation of RE hydroxides does not occur, and performed rigorous solid characterization. The second experiment was designed identically except for using hydroxyapatite (HAP) crystals as the P source at pH constrained by the dissolved P. Hydrated RE phosphate that precipitated at pH 3 after 3 days was classified into three groups: $\text{LREPO}_{4,\text{hyd}}$ (La \rightarrow Gd) containing each REE from La-Gd, $\text{MREPO}_{4,\text{hyd}}$ (Tb \rightarrow Ho), and $\text{HREPO}_{4,\text{hyd}}$ (Er \rightarrow Lu). The latter two groups included increasing fractions of an amorphous component with increasing ionic radius, which was associated with non-coordinated water. $\text{RE}_{\text{all}}\text{PO}_{4,\text{hyd}}$ that contains all lanthanides except Pm transformed to rhabdophane structure over 30 days of aging. In the experiments using HAP, light REEs were preferentially distributed into nano-crystals, which can potentially constrain initial RE distributions in aqueous phase. Consequently, the mineralogical properties of hydrous RE phosphates forming at ambient temperature depend on the aging, the pH of the solution, and the average ionic radii of REE, similarly to the well-crystalline RE phosphates.

Keywords: rare earth elements; hydrated rare earth phosphate; apatite; nanoparticle; TEM

1. Introduction

Rare-earth (RE) elements (REEs), such as the lanthanides (La-Lu), are important rare metals in geological resources, and commonly used for technological application owing to their fluorescent, catalytic, and magnetic properties [1]. REEs are also potential fission products and used as surrogates for trivalent actinides in various experimental studies in nuclear chemistry [2–4]. Among a variety of REE-bearing minerals, RE phosphate is one of the important REE hosts that have further applications to phosphors, though post-heat treatment is required [1].

Crystalline RE phosphates occur in four different structures: monazite (light REPO_4 ; $P2_1/n$), rhabdophane (light $\text{REPO}_4 \cdot n\text{H}_2\text{O}$; $P6_222$ or $C2$), xenotime (heavy REPO_4 ; $I4_1/amd$), and churchite (heavy $\text{REPO}_4 \cdot n\text{H}_2\text{O}$; $I2/a$) [5–8]. In the crust (granite, metamorphic and/or metasomatic rocks, and pegmatite), monazite and xenotime are the stable phases for light REE and heavy REE, respectively, while rhabdophane and churchite occurrences are almost exclusively encountered in soil [9–13].

The structure depends on physico-chemical parameters such as pH, reaction time, and temperature [14–16]. Ionic radii also influence the crystal structure and morphology. Although the previous studies have reported on the mineralogical properties of all four types of RE phosphates and their application to accommodate foreign cations [17,18], these studies were mainly concerned with the well-crystalline phase formed at elevated temperatures at acidic pH ~ 1 , e.g., [16,19]. The crystal chemical property of the hydrous RE phosphates that formed at ambient temperature has not

been explored in detail. In addition, recent studies reported a novel synthesis of RE phosphate nanocrystals in P-free solution using microorganisms that release P from cell interiors at pH 3–5 at room temperature [20,21]; however, the electron diffraction pattern revealed vague patterns with diffused diffraction maxima owing to the presence of amorphous matter, which prevents the full identification of these nanoparticles. Hence, the first half of the present study reports a systematic characterization of hydrated RE phosphates, $\text{REPO}_{4,\text{hyd}}$, that formed at ambient temperature to understand their crystal-chemical properties. The formation of RE hydroxides formation was suppressed by using the pH condition of <6 in the present experiment.

In geological media, RE phosphates occur primarily as an accessory mineral such as monazite and xenotime, and the secondary precipitates of RE phosphates such as rhabdophane frequently play a key role as an indicative of various geochemical signatures such as for estimating paleo-environment [22,23] and migration of actinides such as Pu in the Oklo natural fission reactor [17,18,24–29]. The secondary RE phosphates commonly occur in weathered profiles in association with original phosphate minerals, such as apatite, which acts as a source of phosphorus (P) and provides unique reaction interfaces for the formation of secondary phosphates such as epitaxial growth and pseudomorphism [30]; however, the effects of the substrates has not been evaluated for the formation of hydrous RE phosphate. Thus, the second half of the present study demonstrates the time-course of the formation process of hydrated RE phosphates, $\text{REPO}_{4,\text{hyd}}$, over the HAP crystal at ambient temperatures at varying pHs constrained by dissolved phosphate to elucidate the evolution of secondary RE phosphate at the interfaces and the REE fractionation between solution and solid.

2. Materials and Methods

2.1. $\text{REPO}_{4,\text{hyd}}$ Precipitation from Aqueous Trivalent REE and Phosphate in Solution

In the present study, RE_i refers to phases containing individual La-Lu elements but excludes Pm, and RE_{all} refers to phases containing all La-Lu elements except for Pm. To simplify the discussion, Sc and Y were not included in the present experiment. A series of hydrated RE phosphates, $\text{RE}_i\text{PO}_{4,\text{hyd}}$ (where RE = La-Lu except for Pm) were synthesized from aqueous solutions. The reactants used as starting materials were $\text{La}(\text{NO}_3)_3 \cdot 6\text{H}_2\text{O}$ (99.9%), $\text{Ce}(\text{NO}_3)_3 \cdot 6\text{H}_2\text{O}$ (98%), $\text{Pr}(\text{NO}_3)_3 \cdot x\text{H}_2\text{O}$ (99.5%), $\text{Nd}(\text{NO}_3)_3 \cdot 6\text{H}_2\text{O}$ (99.5%), $\text{Sm}(\text{NO}_3)_3 \cdot 6\text{H}_2\text{O}$ (99.5%), $\text{Gd}(\text{NO}_3)_3 \cdot 6\text{H}_2\text{O}$ (99.5%), $\text{Dy}(\text{NO}_3)_3 \cdot 6\text{H}_2\text{O}$ (99.5%), $\text{Ho}(\text{NO}_3)_3 \cdot x\text{H}_2\text{O}$ (99.5%), $\text{Er}(\text{NO}_3)_3 \cdot x\text{H}_2\text{O}$ (99.5%), and $\text{Yb}(\text{NO}_3)_3 \cdot x\text{H}_2\text{O}$ (99.9%) supplied by Wako Pure Chemical (Osaka, Japan), $\text{Eu}(\text{NO}_3)_3 \cdot 6\text{H}_2\text{O}$ (99.9%) and $\text{Tb}(\text{NO}_3)_3 \cdot 6\text{H}_2\text{O}$ (99.9%) supplied by Strem Chemicals (Newburyport, MA, USA), $\text{Tm}(\text{NO}_3)_3 \cdot x\text{H}_2\text{O}$ (99.9%) supplied by Alfa Aesar (Ward Hill, MA, USA), and $\text{Lu}(\text{NO}_3)_3 \cdot 4\text{H}_2\text{O}$ (99.95%) supplied by Kanto Chemical (Tokyo, Japan). A $0.1 \text{ mol} \cdot \text{L}^{-1}$ RE^{3+} solution was prepared for each REE by dissolving the reactants in ultrapure water (Milli-Q[®], Merck Millipore, Billerica, MA, USA). The pH of each solution was adjusted to $\text{pH } 3.0 \pm 0.1$ with NaOH and HNO_3 using a pH meter (Toko TXP-999i, Tokyo, Japan) with an electrode (Toko PCE108CW-SR). The margin of error in the pH measurements was within 0.1 pH units. In addition, 10 mL of a $0.1 \text{ mol} \cdot \text{L}^{-1}$ NaH_2PO_4 (Wako Pure Chemical) aqueous solution adjusted to $\text{pH } 9.0 \pm 0.1$ was added to 10 mL of a $0.1 \text{ mol} \cdot \text{L}^{-1}$ RE solution with continuous stirring, and the pH was adjusted to 3.0 ± 0.1 . The solutions were shaken by a rotary shaker for 3 days at room temperature. The suspensions were filtered with an Omnipore membrane filter with a pore size of $0.1 \mu\text{m}$ (Merck Millipore JVWP04700, Billerica, MA, USA) and rinsed with ultrapure water. The precipitates were dried in air at room temperature. $\text{RE}_{\text{all}}\text{PO}_{4,\text{hyd}}$ was synthesized using the same procedure as $\text{RE}_i\text{PO}_{4,\text{hyd}}$ and a solution with a total RE concentration of $0.1 \text{ mol} \cdot \text{L}^{-1}$ (RE = La-Lu except Pm), in which the concentration of each REE was set to $7.1 \text{ mmol} \cdot \text{L}^{-1}$.

To evaluate the effects of crystal aging, $\text{RE}_i\text{PO}_{4,\text{hyd}}$ (RE = La, Tb, Dy, Ho, and Yb) and $\text{RE}_{\text{all}}\text{PO}_{4,\text{hyd}}$ were reacted for an extended duration ranging from 3 to 30 days. The effect of pH was examined in the case of $\text{LaPO}_{4,\text{hyd}}$ formation by varying the pH from 1 to 5. $\text{LaPO}_{4,\text{hyd}}$ was synthesized at pH 1 by pouring 10 mL of $0.1 \text{ mol} \cdot \text{L}^{-1}$ NaH_2PO_4 into 10 mL of $0.1 \text{ mol} \cdot \text{L}^{-1}$ $\text{La}(\text{NO}_3)_3$. The pH of the NaH_2PO_4 and $\text{La}(\text{NO}_3)_3$ solutions were adjusted beforehand to 9.0 ± 0.1 and 1.1, respectively, to account for

the number of protons that would be released to the solution during the reaction. For synthesis at pH 5, 10 mL of $0.1 \text{ mol}\cdot\text{L}^{-1}$ NaH_2PO_4 was poured into 10 mL of $0.1 \text{ mol}\cdot\text{L}^{-1}$ $\text{La}(\text{NO}_3)_3$, for which the pH values were adjusted beforehand to 12.2 and 5.3, respectively. After mixing the solutions, the pH was subsequently adjusted again to 5.0 ± 0.1 . The same incubation and filtration procedures were performed as for the other $\text{RE}_i\text{PO}_{4,\text{hyd}}$ phases.

Additional experiments were performed to investigate the thermal stability of $\text{RE}_i\text{PO}_{4,\text{hyd}}$ formed at room temperature. $\text{RE}_i\text{PO}_{4,\text{hyd}}$ (RE = Tb, Dy, Ho, and Yb) and $\text{RE}_{\text{all}}\text{PO}_{4,\text{hyd}}$ synthesized from a solution at pH 3 for 3 days were annealed at 70, 120, 200, 300, 400, or 500 °C for 1 h in a muffle furnace (Yamato Scientific FM38, Tokyo, Japan).

2.2. $\text{REPO}_{4,\text{hyd}}$ Formation on HAP Crystals

RE^{3+} solutions at a concentration of $2.0 \text{ mmol}\cdot\text{L}^{-1}$ (RE = La, Tb, Yb) were prepared by dissolving $\text{RE}(\text{NO}_3)_3\cdot n\text{H}_2\text{O}$ in Milli-Q® water, which was adjusted to a pH of 5 using HNO_3 . 0.2 g of synthetic HAP in the form of $\text{Ca}_5(\text{PO}_4)_3\text{OH}$ powder (Wako Pure Chemical) was added to 100 mL of the RE^{3+} solutions at room temperature. The HAP grains are rod-shaped, with approximate dimensions of $1.5 \mu\text{m} \times 300 \text{ nm}$ and a specific surface area of $6.31 \text{ m}^2\cdot\text{g}^{-1}$ [30]. The S/V ratio (where S is the apatite surface area and V is the volume of solution) was $1.3 \times 10^2 \text{ cm}^{-1}$ in these experiments. The suspensions of HAP powders were gently agitated using a magnetic stirrer for 1, 3, 9, and 24 h and 3 and 10 days. The solution pH was measured for each duration. The precipitate was collected by centrifugation at 3000 rpm for 10 min at 25 °C, washed with ultrapure water, and dried in air at room temperature. The supernatants remaining after centrifugation were filtered under reduced pressure with an Omnipore membrane filter with a pore size of $0.025 \mu\text{m}$ (Merck Millipore VSWP04700), which was small enough to separate the precipitates from the supernatant. $\text{RE}_{\text{all}}\text{PO}_{4,\text{hyd}}$ was also synthesized on HAP through the same procedure using a solution with a total RE concentration of $2.0 \text{ mmol}\cdot\text{L}^{-1}$ (RE = La-Lu except Pm), in which the concentration of each REE was $0.14 \text{ mmol}\cdot\text{L}^{-1}$.

2.3. Analytical Methods

The crystal structures of $\text{RE}_i\text{PO}_{4,\text{hyd}}$ (RE = La-Lu) and $\text{RE}_{\text{all}}\text{PO}_{4,\text{hyd}}$ prepared from solution at room temperature were determined using powder X-ray diffraction analysis (XRD, Rigaku MultiFlex, Tokyo, Japan or Rigaku SmartLab). The analysis was conducted using Cu $K\alpha$ radiation ($\lambda = 1.5418 \text{ \AA}$) at 40 kV and 40 mA for the MultiFlex instrument, and at 40 kV and 30 mA for the SmartLab instrument in a scan range of $2\theta = 10^\circ\text{--}63^\circ$ with a scan speed of 2° per min. A non-reflective silicon (111) holder was used to hold the specimens. The $\text{REPO}_{4,\text{hyd}}$ that formed on HAP crystals was analyzed using the SmartLab XRD in a scan range of $10^\circ\text{--}50^\circ$ using a SiO_2 glass plate as a specimen holder. Each spectrum was smoothed with a modified Savitzky–Golay filter and the linear background was subtracted using JADE 7 software (Materials Data Incorporated, Livermore, CA, USA). Subsequently, peak separation and fitting were conducted using the same software to calculate the crystallite size from the Scherrer equation:

$$D = \frac{K\lambda}{\beta \cos \theta} \quad (1)$$

where D , K , λ , β , and θ refer to the crystallite size (\AA), the Scherrer constant (in this study $K = 0.9$), the wavelength of X-rays (1.5418 \AA), the full-width at half maximum of the peak (rad), and the Bragg angle at the peak (rad), respectively.

$\text{RE}_i\text{PO}_{4,\text{hyd}}$ (RE = La-Lu) and $\text{RE}_{\text{all}}\text{PO}_{4,\text{hyd}}$ prepared from solution at pH 3 for 3 days and 30 days were analyzed by Fourier transform infrared spectroscopy (FT-IR) using KBr disks (1 mg sample/100 mg KBr, 10 mm in diameter). Spectra were recorded at a resolution of 4 cm^{-1} by summation of 32 scans.

Thermogravimetry–differential thermal analysis (TG–DTA) was performed on $\text{RE}_i\text{PO}_{4,\text{hyd}}$ (RE = La-Lu) and $\text{RE}_{\text{all}}\text{PO}_{4,\text{hyd}}$ prepared from solution at pH 3 for a duration of 3 days. Furthermore, $\text{RE}_i\text{PO}_{4,\text{hyd}}$ (RE = La, Tb, Yb) and $\text{RE}_{\text{all}}\text{PO}_{4,\text{hyd}}$ were reacted at pH 3 for 30 days and were analyzed to

investigate the effect of aging. Each specimen was heated to 500 °C at a heating rate of 10 °C/min and then held for 10 min at 500 °C under a nitrogen gas flow of 250 mL/min using α -alumina as a reference material (Hitachi TG/DTA7300, Tokyo, Japan).

The supernatant after filtration was analyzed to obtain the concentrations of RE (RE = La-Lu), Ca, and P using inductively coupled plasma atomic emission spectroscopy (ICP-AES, PerkinElmer Optima 530 DV, Waltham, MA, USA).

High-resolution transmission electron microscopy (HRTEM), selected-area electron diffraction (SAED), high-angle annular dark-field scanning transmission electron microscopy (HAADF-STEM), and energy dispersive X-ray spectroscopy (EDS) were performed for all precipitate samples obtained in the syntheses using a JEOL JEM-ARM200F (Tokyo, Japan) with an accelerating voltage of 200 kV. The spherical aberration coefficient C_s is ~ 0 mm. The contrast in HAADF-STEM mode correlates with the mass and thickness of the target material [31]. TEM specimens were prepared by placing drops of a suspension of the synthesized precipitates onto a holey carbon mesh supported by a Cu grid.

3. Results

3.1. XRD Analysis

XRD patterns for $RE_iPO_{4,hyd}$ (RE = La-Lu except Pm) and $RE_{all}PO_{4,hyd}$ reacted at pH 3 for 3 days are shown in Figure 1a. The peak positions of $RE_iPO_{4,hyd}$ (RE = La-Gd except Pm) correspond well, with a slight peak shift, to the structure of rhabdophane [8]. The patterns for $RE_iPO_{4,hyd}$ (RE = Tb-Lu) and $RE_{all}PO_{4,hyd}$ could not be identified due to the broadened peaks and lack of matching structures. Although a few of the $RE_iPO_{4,hyd}$ (RE = Er-Lu) peaks appear to be similar to those of xenotime [5], the patterns lack a (200) peak and, thus, the structures were not determined convincingly. Furthermore, the patterns for $RE_iPO_{4,hyd}$ (RE = Tb-Ho) display intermediate profiles between those of $RE_iPO_{4,hyd}$ (RE = La-Gd except Pm) and $RE_iPO_{4,hyd}$ (RE = Er-Lu). Based on the structural characteristics indicated by XRD analysis in this study, the structure of the $RE_iPO_{4,hyd}$ precipitates are classified as $LREPO_{4,hyd}$ for phases containing RE = La-Gd, $MREPO_{4,hyd}$ containing RE = Tb-Ho, and $HREPO_{4,hyd}$ containing RE = Er-Lu, respectively. In $LREPO_{4,hyd}$, which has a rhabdophane structure, the coordination numbers (CNs) of RE^{3+} ions are one third eight-fold and two-thirds nine-fold [8], resulting in an average CN of 8.7. RE^{3+} in $MREPO_{4,hyd}$ and $HREPO_{4,hyd}$ can be considered to have eight-fold coordination because the CN of xenotime and churchite is eight-fold. Based on the CNs of all possible $RE_iPO_{4,hyd}$ phases, the average ionic radius of $RE_{all}PO_{4,hyd}$ containing all RE (RE = La-Lu except Pm) is calculated to be 1.07 Å, which lies just between that of Gd (CN = 8.7, 1.09 Å) and of Tb (CN = 8, 1.04 Å) [32].

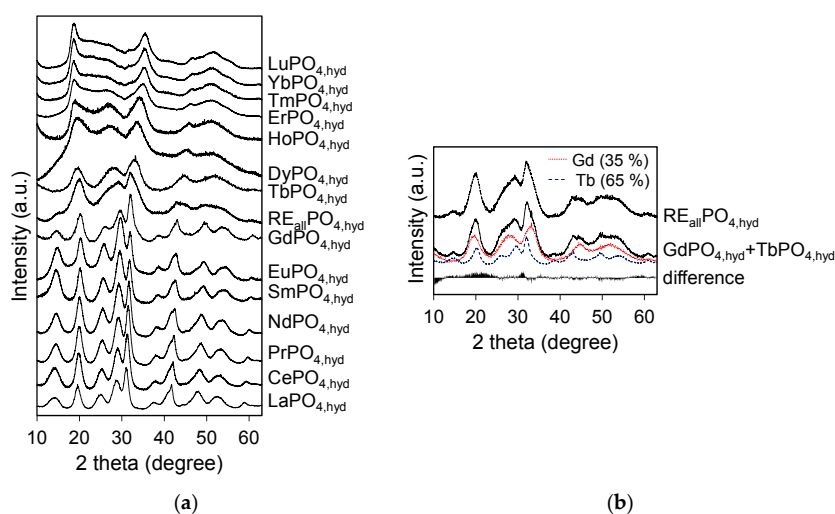


Figure 1. Cont.

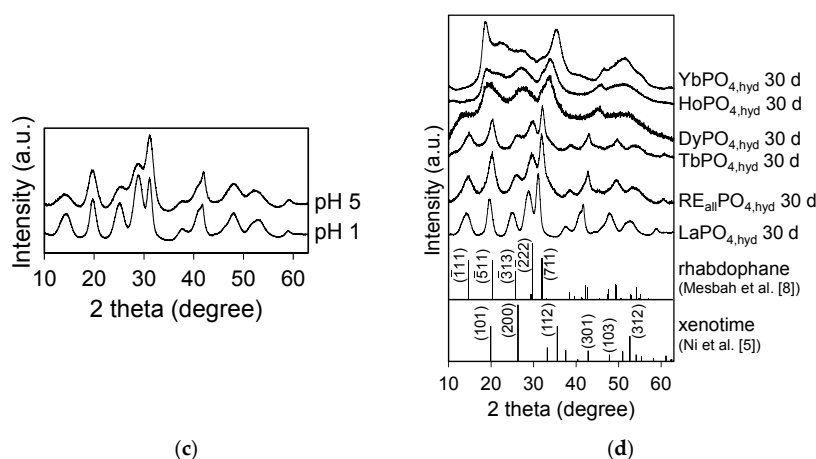


Figure 1. (a) XRD patterns of RE_iPO_{4,hyd} (RE = La-Lu except Pm) and RE_{all}PO_{4,hyd} reacted at pH 3 for 3 days at room temperature. The patterns are arranged in order of increasing effective ionic radius from top to bottom; (b) comparison between XRD pattern of RE_{all}PO_{4,hyd} and a calculated linear combination of the patterns of GdPO_{4,hyd} + TbPO_{4,hyd}, which indicate proportions of 35% GdPO_{4,hyd} and 65% TbPO_{4,hyd} in the pattern based on a least-squares fitting method. The difference in the profiles between RE_{all}PO_{4,hyd} and the calculation is also shown; (c) XRD patterns of LaPO_{4,hyd} reacted at pH 1 and 5 for 3 days; (d) XRD patterns of RE_iPO_{4,hyd} (RE = La, Tb, Dy, Ho, Yb) and RE_{all}PO_{4,hyd} reacted at pH 3 for 30 days, accompanied by XRD patterns of rhabdophane-(Sm) and xenotime-(Lu) with Miller indexes from [5,8].

The XRD pattern of RE_{all}PO_{4,hyd} correlates to a combination of the GdPO_{4,hyd} and TbPO_{4,hyd} patterns. A linear combination of these two profiles indicates volume fractions of 35% GdPO_{4,hyd} structure and 65% TbPO_{4,hyd} structure (Figure 1b).

The effect of pH on LaPO_{4,hyd} precipitates are shown in Figure 1a,c. The full width at half maximum (FWHM) of each peak becomes smaller as the pH lowers.

In the aging experiments, there was little difference in the XRD profiles between 3 and 30 days for RE_iPO_{4,hyd} (RE = La, Dy, Ho, and Yb); however, the structures of RE_{all}PO_{4,hyd} and TbPO_{4,hyd} changed significantly to become rhabdophane-structured after 30 days of aging (Figure 1a,d). In the DyPO_{4,hyd} pattern, a small peak corresponding to the (111) plane of rhabdophane appeared after 30 days of reaction, although the other peaks remained unchanged. The crystallite sizes of LaPO_{4,hyd} calculated on the basis of the XRD patterns in Figure 1 using Scherrer equation are clearly a function of pH and the aging period (Figure 2a,b) and are summarized in Table 1.

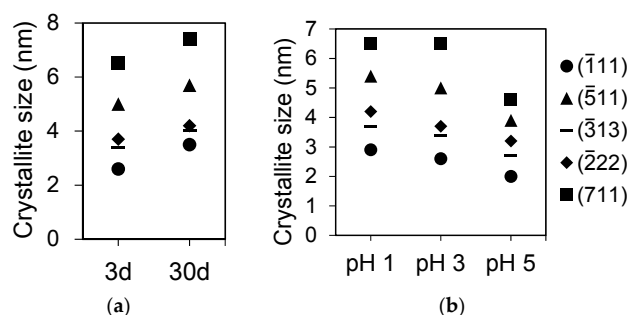


Figure 2. Crystallite sizes of LaPO_{4,hyd} calculated based on the Scherrer equation using JADE software. (a) LaPO_{4,hyd} formed at pH 3 after 3 or 30 days; (b) LaPO_{4,hyd} formed at pH values of 1, 3, and 5 after 3 days.

The calculated lattice volume of LREPO_{4,hyd} reacted at a pH of 3 for 3 days are plotted as a function of the effective ionic radius in Figure 3a by fitting the (111), (511), (313), (222), and (711) peaks to

the peaks of the rhabdophane structure using the JADE software. The calculated lattice parameters are summarized in Table 2. The calculated lattice volume displays a positive linear correlation with the effective ionic radius, indicating that the crystal lattice shrinks uniformly as the ionic radius decreases (Figure 3a). The lattice volumes calculated in the present experiment are larger than that of well-crystalline rhabdophane structure reported in [8], most likely owing to the presence of more water molecules in the structure of $\text{LREPO}_{4,\text{hyd}}$.

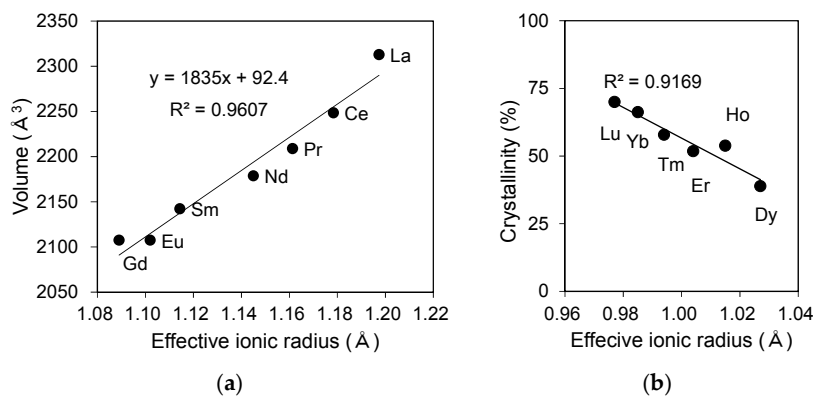


Figure 3. (a) Lattice volume of $\text{LREPO}_{4,\text{hyd}}$ (RE = La-Gd) calculated using JADE software, accompanied by a linear regression line; (b) crystallinity of $\text{RE}_i\text{PO}_{4,\text{hyd}}$ (RE = Dy-Lu) determined from XRD patterns calculated using JADE. These values indicate the intensity percentage of a crystalline peak I_c , which is obtained by subtracting the intensity of the amorphous halo I_a appearing at a 2-theta value of 20–30 degrees as: $\text{Crystallinity (\%)} = I_c / (I_c + I_a)$.

Table 1. Crystallite size of $\text{LaPO}_{4,\text{hyd}}$ samples formed under four different conditions. The calculation was performed for five major peaks in the XRD pattern using the JADE software based on the Scherrer equation with a Scherrer constant K of 0.9.

| Miller Index | $\text{LaPO}_{4,\text{hyd}}$ Crystallite Size (nm) | | | |
|--------------|--|---------------|--------------|--------------|
| | pH 3, 3 days | pH 3, 30 days | pH 1, 3 days | pH 5, 3 days |
| (11) | 2.6 | 3.5 | 2.9 | 2.0 |
| (11) | 5.0 | 5.7 | 5.4 | 3.9 |
| (13) | 3.4 | 4.0 | 3.7 | 2.7 |
| (22) | 3.7 | 4.2 | 4.2 | 3.2 |
| (711) | 6.5 | 7.4 | 6.5 | 4.6 |

Table 2. Lattice parameters a , b , c and β , and lattice volume for $\text{RE}_i\text{PO}_{4,\text{hyd}}$ (RE = La-Gd) calculated based on the peaks in the XRD patterns using the JADE software.

| REE | Effective Ionic Radius (Å) ¹ | Lattice Parameter (Å) | | | | Lattice Volume (Å ³) |
|-----|---|-----------------------|------|-------|---------|----------------------------------|
| | | a | b | c | β | |
| La | 1.197 | 29.17 | 7.19 | 12.29 | 116.3 | 2313 |
| Ce | 1.178 | 28.50 | 7.22 | 12.13 | 115.7 | 2249 |
| Pr | 1.161 | 28.61 | 7.06 | 12.14 | 115.8 | 2209 |
| Nd | 1.145 | 28.48 | 7.04 | 12.07 | 115.8 | 2179 |
| Sm | 1.114 | 28.34 | 6.99 | 12.01 | 115.8 | 2142 |
| Eu | 1.102 | 27.93 | 7.02 | 11.91 | 115.5 | 2108 |
| Gd | 1.089 | 27.89 | 7.06 | 11.85 | 115.5 | 2108 |

¹ The effective ionic radius $r = 1/3 r_{\text{CN}8} + 2/3 r_{\text{CN}9}$.

The crystallinity of $\text{RE}_i\text{PO}_{4,\text{hyd}}$ (RE = Dy-Lu) was calculated based on the profile fitting of amorphous halos in the XRD patterns (Figure S2, Table 3) and is plotted in Figure 3b as a function of effective ionic radius. The results indicate that $\text{DyPO}_{4,\text{hyd}}$ has the largest amorphous volume and that the amorphous fraction linearly decreases towards $\text{LuPO}_{4,\text{hyd}}$.

The XRD patterns of $\text{RE}_i\text{PO}_{4,\text{hyd}}$ (RE = Tb, Ho, Dy, and Yb) and $\text{RE}_{\text{all}}\text{PO}_{4,\text{hyd}}$ obtained from the annealing experiments are summarized in Figure 4. $\text{TbPO}_{4,\text{hyd}}$ transformed to a monazite structure at 400 °C with small peaks occurring at a 2θ value around 30°, as indicated by the circle. $\text{DyPO}_{4,\text{hyd}}$ appeared to transform to a xenotime structure at 400 °C, as indicated by the appearance of small peaks at a 2θ value around 25.8°. $\text{HoPO}_{4,\text{hyd}}$ and $\text{YbPO}_{4,\text{hyd}}$ also transformed to a xenotime structure at around 300 and 200 °C, respectively. $\text{RE}_{\text{all}}\text{PO}_{4,\text{hyd}}$ appeared to retain its initial structure up to 200 °C and then transformed to a rhabdophane structure, which was retained up to 500 °C. In contrast, $\text{TbPO}_{4,\text{hyd}}$ did not become rhabdophane-structured but directly transformed to a monazite structure when annealed in air. The thermal behavior of $\text{TbPO}_{4,\text{hyd}}$ is different from that observed in the aging experiments, in which the structure simply changed to that of rhabdophane.

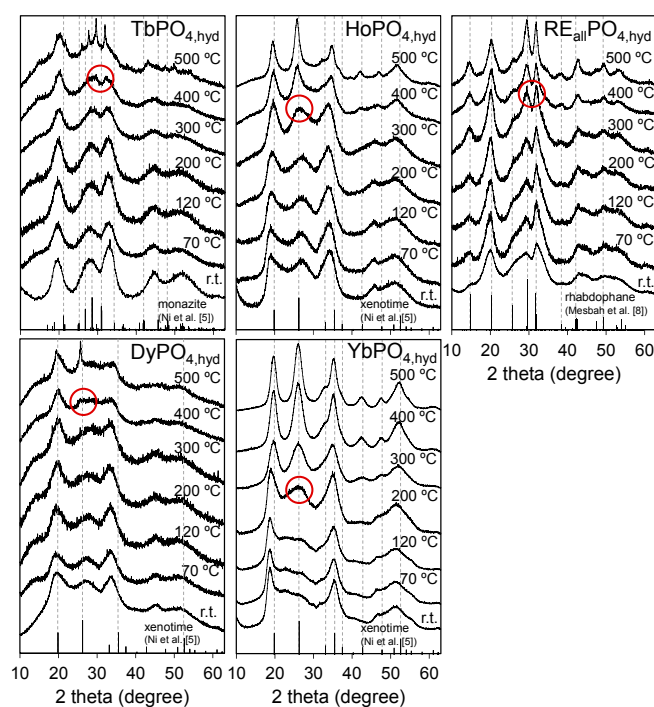


Figure 4. Transition in XRD patterns of $\text{RE}_i\text{PO}_{4,\text{hyd}}$ (RE = Tb, Dy, Ho, Yb) and $\text{RE}_{\text{all}}\text{PO}_{4,\text{hyd}}$ formed at pH 3 for 3 days at room temperature during annealing up to 500 °C. The patterns of each $\text{REPO}_{4,\text{hyd}}$ are accompanied by the spectrum of the ideal RE phosphate minerals; rhabdophane, monazite, and xenotime, based on [5,8], where r.t. represents room temperature. A circle indicates peaks exhibiting structural transformation.

Table 3. The results of quantification of the crystallinity of $\text{RE}_i\text{PO}_{4,\text{hyd}}$ (RE = Dy-Lu) calculated using the JADE software.

| REE | Effective Ionic Radius (Å) ¹ | Crystallinity (%) |
|-----|---|-------------------|
| Dy | 1.027 | 38.9 |
| Ho | 1.015 | 53.9 |
| Er | 1.004 | 51.8 |
| Tm | 0.994 | 57.9 |
| Yb | 0.985 | 66.2 |
| Lu | 0.977 | 70.0 |

¹ The effective ionic radius from [32].

3.2. FT-IR Analysis

Infrared spectra for $\text{RE}_i\text{PO}_{4,\text{hyd}}$ (RE = La-Lu except Pm) and $\text{RE}_{\text{all}}\text{PO}_{4,\text{hyd}}$ reacted at pH 3 for 3 days are shown in Figure 5a. Two bands at $520\text{--}650\text{ cm}^{-1}$ (labeled 1 and 2) correspond to the asymmetric P–O bending vibration, ν_3 , while the bands at $1000\text{--}1100\text{ cm}^{-1}$ (labeled 3 and 4) correspond to the antisymmetric P–O stretching vibration, ν_4 [33–35]. Bands 3 and 4 are not clearly separated for $\text{LREPO}_{4,\text{hyd}}$. The symmetric stretching mode ν_1 , which typically appears as a small absorption band at $\sim 966\text{--}985\text{ cm}^{-1}$ [36] and the bending vibration ν_2 were not observed, possibly because those bands were superimposed in the ν_3 and ν_4 regions for the hydrated RE phosphates [35]. The wavenumbers of band 4 in the ν_3 region plotted as a function of the effective ionic radius (Figure 5b and Table 4) exhibit a linear decrease with increasing ionic radius for $\text{LREPO}_{4,\text{hyd}}$ and $\text{HREPO}_{4,\text{hyd}}$, while $\text{MREPO}_{4,\text{hyd}}$ and $\text{RE}_{\text{all}}\text{PO}_{4,\text{hyd}}$ did not exhibit such trends. The broad bands at $\sim 1600\text{ cm}^{-1}$ (band 5) and at $\sim 3000\text{--}3500\text{ cm}^{-1}$ (band 6) are derived from coordinated H_2O [34]. Nitrate impurities derived from the initial REE reagents produce the band at $\sim 1380\text{ cm}^{-1}$.

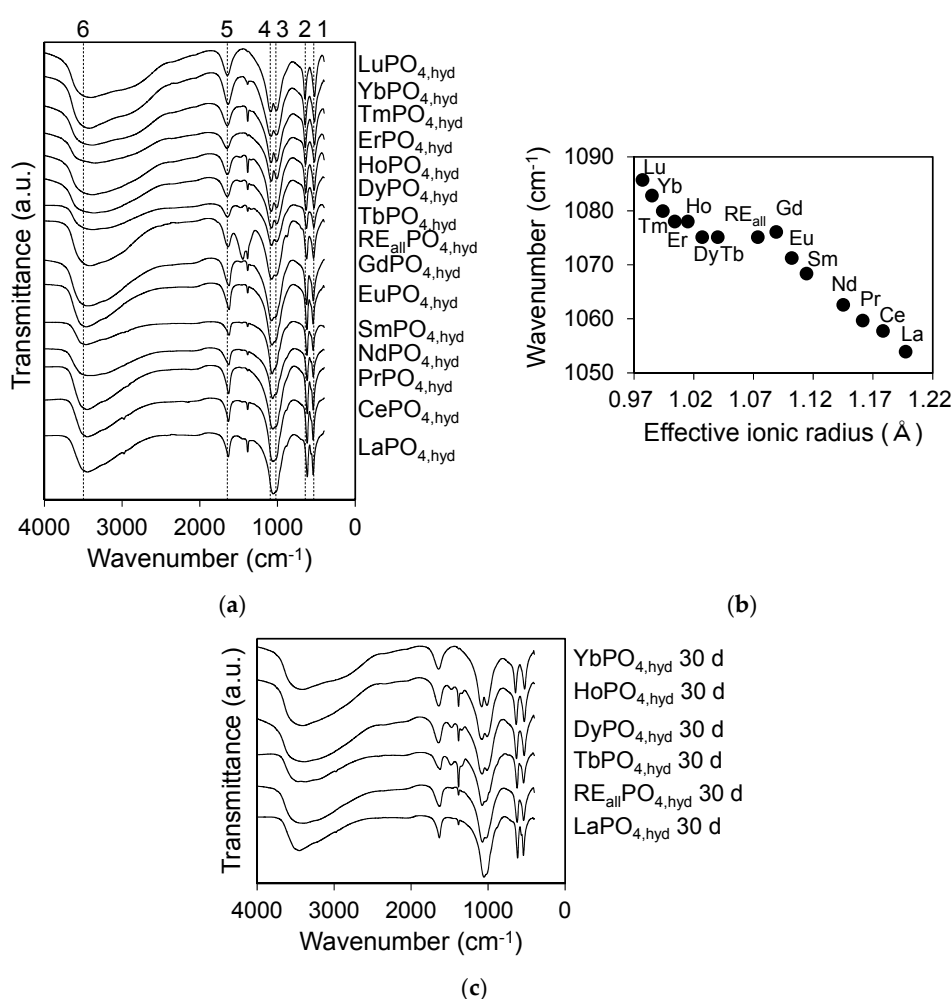


Figure 5. (a) IR spectra of $\text{RE}_i\text{PO}_{4,\text{hyd}}$ (RE = La-Lu) and $\text{RE}_{\text{all}}\text{PO}_{4,\text{hyd}}$ reacted at pH 3 for 3 days. The bands labeled 1–2, 3–4, 5, and 6 correspond to the P–O bending, P–O antisymmetric stretching, O–H bending, and O–H stretching vibrations, respectively; (b) a diagram showing the wavenumber of the P–O antisymmetric stretching vibration (labeled 4 in Figure 5a) of $\text{RE}_i\text{PO}_{4,\text{hyd}}$ (RE = La-Lu) and $\text{RE}_{\text{all}}\text{PO}_{4,\text{hyd}}$ as a function of the effective ionic radius; (c) IR spectra of $\text{RE}_i\text{PO}_{4,\text{hyd}}$ (RE = La, Tb, Dy, Ho, Yb) and $\text{RE}_{\text{all}}\text{PO}_{4,\text{hyd}}$ reacted at pH 3 for 30 days.

Table 4. List of the wavenumber of band 4 that corresponds to P–O antisymmetric stretching vibration, ν_4 in the FT-IR spectra obtained for RE_iPO_4 (RE = La–Lu) and $\text{RE}_{\text{all}}\text{PO}_{4,\text{hyd}}$ from FT-IR spectra.

| REE | Effective Ionic Radius (Å) ¹ | Wavenumber (cm ^{−1}) |
|-------------------|---|--------------------------------|
| La | 1.197 | 1053.9 |
| Ce | 1.178 | 1057.8 |
| Pr | 1.161 | 1059.7 |
| Nd | 1.145 | 1062.6 |
| Sm | 1.114 | 1068.4 |
| Eu | 1.102 | 1071.3 |
| Gd | 1.089 | 1076.1 |
| RE _{all} | 1.074 | 1075.1 |
| Tb | 1.040 | 1075.1 |
| Dy | 1.027 | 1075.1 |
| Ho | 1.015 | 1078.0 |
| Er | 1.004 | 1078.0 |
| Tm | 0.994 | 1079.9 |
| Yb | 0.985 | 1082.8 |
| Lu | 0.977 | 1085.7 |

¹ Effective ionic radius: $r_{\text{La-Gd}} = 1/3 r_{\text{CN8}} + 2/3 r_{\text{CN9}}$, $r_{\text{Tb-Lu}} = r_{\text{CN8}}$, and r_{all} is the average of $r_{\text{La-Lu}}$.

FT-IR spectrum of the aged $\text{TbPO}_{4,\text{hyd}}$ and $\text{RE}_{\text{all}}\text{PO}_{4,\text{hyd}}$ appeared to be similar to that of $\text{LaPO}_{4,\text{hyd}}$, especially at bands 3 and 4 (Figure 5c). These FT-IR results concur with the XRD analyses, i.e., they indicate a change in the structures of $\text{RE}_{\text{all}}\text{PO}_{4,\text{hyd}}$ and $\text{TbPO}_{4,\text{hyd}}$ to a rhabdophane structure after 30 days of aging in solution.

3.3. TG-DTA Analysis

Derivatives of the TG (DTG) and DTA spectra for $\text{RE}_i\text{PO}_{4,\text{hyd}}$ (RE = La–Lu) and $\text{RE}_{\text{all}}\text{PO}_{4,\text{hyd}}$ reacted at a pH of 3 for 3 days are shown in Figure 6. $\text{LREPO}_{4,\text{hyd}}$ and $\text{HREPO}_{4,\text{hyd}}$ display a two-step dehydration, which is indicated by the presence of a DTG upper peak with an endothermic DTA peak. Assuming that the material remaining after heating to 500 °C entirely comprise anhydrous RE phosphates and the weight loss is derived solely from the dissociation of H_2O in $\text{REPO}_{4,\text{hyd}}$, the amount of dissociated water was calculated for the total heating duration (Figure 7a) and for each dehydration step (Figure 7b,c), and compiled in Table 5. The starting temperature of the second dehydration step was determined by selecting the local minimum of the DTG spectrum or the peak of the DTA spectrum between the first and second dehydration steps. A diagram of the dehydration extent in the first step in $\text{HREPO}_{4,\text{hyd}}$ indicates that the amount of water loss increases as a function of ionic radius (Figure 7b). The amount of water loss in the second dehydration step also appears to exhibit a linear decrease as the ionic radii decrease in $\text{LREPO}_{4,\text{hyd}}$ and $\text{HREPO}_{4,\text{hyd}}$ (Figure 7c). $\text{MREPO}_{4,\text{hyd}}$ and $\text{RE}_{\text{all}}\text{PO}_{4,\text{hyd}}$ each exhibited only one dehydration peak. For these phases, a DTG upper peak and a DTA exothermic peak are present, indicating that crystallization occurred during dehydration.

Table 5. Summary of dehydration or crystallization temperature and the amount of dissociated water n from the $\text{RE}_i\text{PO}_{4,\text{hyd}}$ (RE = La–Lu) and $\text{RE}_{\text{all}}\text{PO}_{4,\text{hyd}}$ during the TG-DTA analysis heated up to 500 °C. The value n corresponds to the number of H_2O molecule per unit formula.

| REE | Effective Ionic Radius (Å) ¹ | Second Dehydration Temperature (°C) | Crystallization Temperature (°C) | Dissociated Water n | | |
|-----|---|-------------------------------------|----------------------------------|-----------------------|-------|--------|
| | | | | Total | First | Second |
| La | 1.197 | 165 | - | 1.95 | 1.30 | 0.66 |
| Ce | 1.178 | 147 | - | 1.71 | 1.03 | 0.68 |
| Pr | 1.161 | 143 | - | 1.86 | 1.14 | 0.72 |
| Nd | 1.145 | 137 | - | 1.76 | 1.00 | 0.76 |
| Sm | 1.114 | 127 | - | 1.54 | 0.80 | 0.73 |
| Eu | 1.102 | 117 | - | 1.58 | 0.75 | 0.83 |
| Gd | 1.089 | 133 | - | 1.96 | 1.13 | 0.83 |

Table 5. Cont.

| REE | Effective Ionic Radius (Å) ¹ | Second Dehydration Temperature (°C) | Crystallization Temperature (°C) | Dissociated Water <i>n</i> | | |
|-------------------|---|-------------------------------------|----------------------------------|----------------------------|-------|--------|
| | | | | Total | First | Second |
| RE _{all} | 1.074 | - | 220 | 2.22 | - | - |
| Tb | 1.040 | - | 300 | 2.24 | - | - |
| Dy | 1.027 | - | 326 | 2.36 | - | - |
| Ho | 1.015 | - | 300 | 2.43 | - | - |
| Er | 1.004 | 178 | - | 2.64 | 1.77 | 0.86 |
| Tm | 0.994 | 169 | - | 2.63 | 1.66 | 0.97 |
| Yb | 0.985 | 150 | - | 2.56 | 1.54 | 1.02 |
| Lu | 0.977 | 160 | - | 2.39 | 1.40 | 0.99 |

¹ Effective ionic radius: $r_{\text{La-Gd}} = 1/3 r_{\text{CN8}} + 2/3 r_{\text{CN9}}$, $r_{\text{Tb-Lu}} = r_{\text{CN8}}$, and r_{all} is the average of $r_{\text{La-Lu}}$.

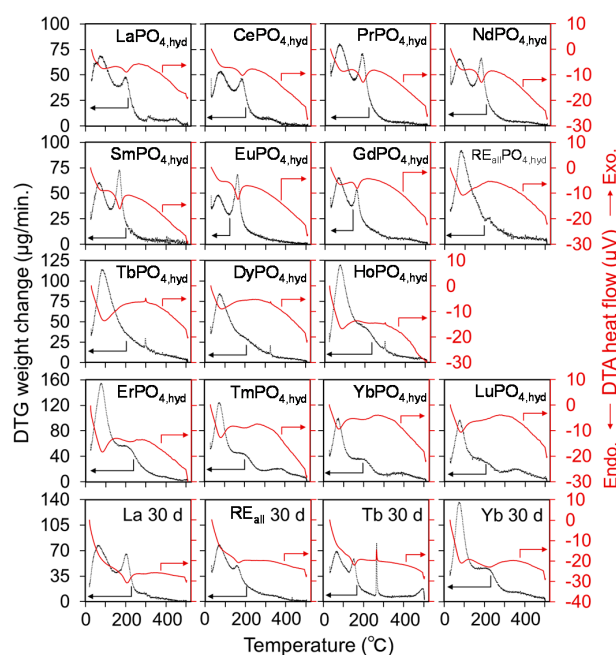


Figure 6. Differential thermogravimetric and thermal spectra of RE_iPO_{4,hyd} (RE = La-Lu) and RE_{all}PO_{4,hyd} reacted at pH 3 for 3 days. RE_iPO_{4,hyd} (RE = La, Tb, Yb) and RE_{all}PO_{4,hyd} reacted for 30 days are also shown. The black dotted line indicates the DTG curve and the red solid line represents the DTA heat flow.

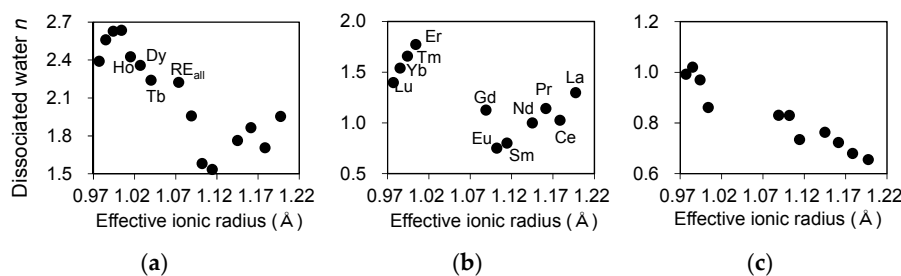


Figure 7. (a) The number of water molecules per formula unit in REPO_{4,hyd} plotted as a function of REE ionic radius determined based on the TG-DTA results (Figure 6); the amounts of water dissociated during (b) the first dehydration step and (c) the second dehydration step calculated for LREPO_{4,hyd} and HREPO_{4,hyd}.

In addition, the DTG and DTA spectra of RE_iPO_{4,hyd} (RE = La, Tb, and Yb) and RE_{all}PO_{4,hyd} after 30 days of reaction time are shown in Figure 6 for comparison with samples measured after

3 days of reaction time. Although $\text{LaPO}_{4,\text{hyd}}$ and $\text{YbPO}_{4,\text{hyd}}$ did not appear significantly different from those samples that had reacted for 3 days, additional dehydration peaks appeared in the spectra of $\text{TbPO}_{4,\text{hyd}}$ and $\text{RE}_{\text{all}}\text{PO}_{4,\text{hyd}}$ reacted for 30 days.

3.4. ICP-AES Analysis

In experiments of HAP dissolution in a solution containing all REEs, the concentrations of RE (RE = La-Lu except Pm), Ca, and P were measured for each duration using ICP-AES. The results are summarized in Table 6 and the total REE concentrations are plotted in Figure 8a as a function of reaction time. The P concentration is under the detection limit for all durations. The Ca concentration increased linearly for periods from 3 to 24 h, whereas the total concentration of all REEs decreased inversely with the Ca concentration. The reaction did not reach equilibrium within the duration of this dissolution experiment (Figure 8a); however, more than 80% of the total initial REE concentration was removed from solution after 240 h.

Figure 8b shows the transition in the patterns of REEs in solution reacted with HAP. The four curves at La-Nd, Sm-Gd, Gd-Ho, and Er-Lu exhibit the lanthanide tetrad effect [37]. Furthermore, more heavy REEs remained in solution compared with light REEs, and this trend becomes more pronounced with reaction time. The possible concentrations of free RE^{3+} , RECO_3^+ , and REOH^{2+} at these experimental conditions were calculated using Geochemist's Workbench using their formation constants [38], and input data of $P_{\text{CO}_2} = 10^{-3.5}$ bar [39] and phosphate free solution. The calculation results clearly demonstrate that the concentration of free RE^{3+} decreases as the ionic radius decreases because the amount of other REE complexes such as RECO_3^+ and REOH^{2+} increase with decreasing ionic radius (Figure 8c,d).

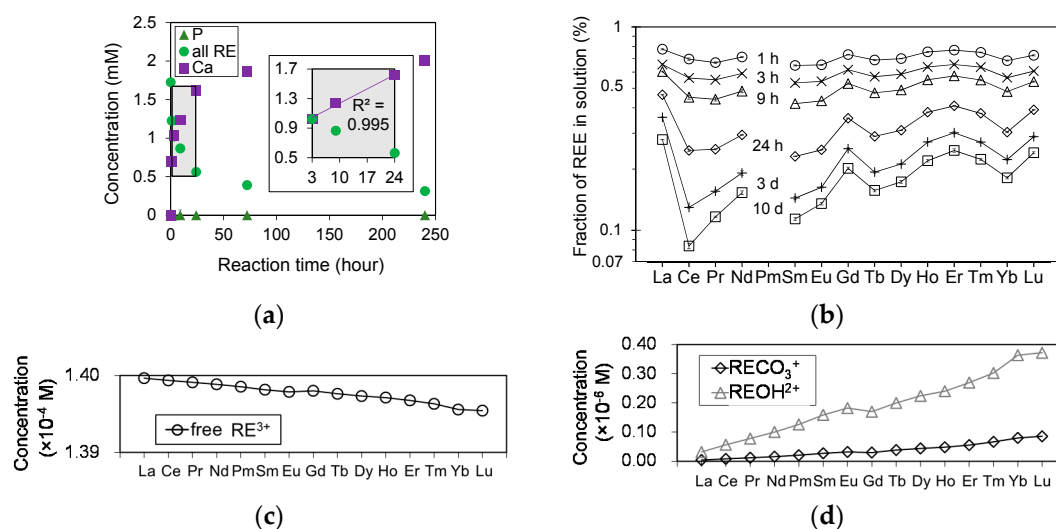


Figure 8. (a) Time-dependent concentrations of P (filled green triangles), Ca (filled purple squares), and all RE (filled light green circles) in solution during the experiment with HAP in contact with a RE^{3+} solution; (b) development of REE patterns in the solution as a function of time. The concentrations were normalized to the initial concentration; (c) thermodynamic calculation of aqueous RE^{3+} species in solution at a pH of 5 under the conditions of the present study. Concentration of free (non-coordinated) RE^{3+} calculated by subtracting the concentration of RECO_3^+ and REOH^{2+} from the initial concentration of RE^{3+} (0.14 mM of each RE^{3+}); (d) the concentrations of RECO_3^+ and REOH^{2+} obtained by multiplying the initial concentrations of RE^{3+} (0.14 mM of each La-Lu), the concentration of CO_3^{2-} or OH^- , and the formation constant $\text{CO}_3\beta_1$ or $\text{OH}\beta_1$ [38]. The concentrations of CO_3^{2-} and OH^- were calculated using Geochemist's Workbench with the thermodynamic database *thermo.dat* and input data of pH 5 and $P_{\text{CO}_2} = 10^{-3.5}$ bar [39].

Table 6. The solution composition determined by ICP-AES at each reaction time during the formation of $\text{RE}_{\text{all}}\text{PO}_{4,\text{hyd}}$, in which HAP crystals were in contact with the solution containing all REEs.

| Reaction Time | Concentration ($\text{mmol}\cdot\text{dm}^{-3}$) | | | | | | | | | | | | | | | | pH |
|---------------|--|------|------|------|------|------|------|------|------|------|------|------|------|------|------------------|----------------|----------------|
| | La | Ce | Pr | Nd | Sm | Eu | Gd | Tb | Dy | Ho | Er | Tm | Yb | Lu | Ca | P ¹ | |
| 0 h | 0.12 | 0.11 | 0.13 | 0.12 | 0.12 | 0.13 | 0.11 | 0.13 | 0.11 | 0.13 | 0.13 | 0.13 | 0.13 | 0.13 | udl ¹ | udl | 5.06 |
| 1 h | 0.10 | 0.08 | 0.09 | 0.09 | 0.08 | 0.08 | 0.08 | 0.09 | 0.08 | 0.10 | 0.10 | 0.10 | 0.09 | 0.10 | 0.70 | udl | 5.16 |
| 3 h | 0.08 | 0.06 | 0.07 | 0.07 | 0.06 | 0.07 | 0.06 | 0.07 | 0.07 | 0.08 | 0.08 | 0.08 | 0.08 | 0.08 | 1.03 | udl | 5.53 |
| 9 h | 0.07 | 0.05 | 0.06 | 0.06 | 0.05 | 0.06 | 0.06 | 0.06 | 0.06 | 0.07 | 0.07 | 0.07 | 0.06 | 0.07 | 1.23 | udl | 5.55 |
| 24 h | 0.06 | 0.03 | 0.03 | 0.04 | 0.03 | 0.03 | 0.04 | 0.04 | 0.03 | 0.05 | 0.05 | 0.05 | 0.04 | 0.05 | 1.62 | udl | 5.63 |
| 3 days | 0.04 | 0.01 | 0.02 | 0.02 | 0.02 | 0.02 | 0.03 | 0.02 | 0.02 | 0.03 | 0.04 | 0.03 | 0.03 | 0.04 | 1.86 | udl | 5.66 |
| 10 days | 0.03 | 0.01 | 0.01 | 0.02 | 0.01 | 0.02 | 0.02 | 0.02 | 0.02 | 0.03 | 0.03 | 0.03 | 0.02 | 0.03 | 2.01 | udl | - ² |

¹ udl: Under detection limits (0.05 ppb for Ca and 15 ppb for P). ² The pH after 10 days was not available.

3.5. TEM Analysis

The grain shapes of $\text{REPO}_{4,\text{hyd}}$ gradually change with ionic radius. HRTEM images show that $\text{RE}_i\text{PO}_{4,\text{hyd}}$ ($\text{RE} = \text{La}, \text{Nd}, \text{Tb}$) and $\text{RE}_{\text{all}}\text{PO}_{4,\text{hyd}}$ form rod-shaped particles of ~ 50 nm in length. $\text{TmPO}_{4,\text{hyd}}$ and $\text{LuPO}_{4,\text{hyd}}$ are spherically shaped with diameters of 10 nm (Figure 9). $\text{DyPO}_{4,\text{hyd}}$ and $\text{HoPO}_{4,\text{hyd}}$ precipitates do not exhibit any specific shape due to their amorphous characteristics. The SAED patterns of $\text{LREPO}_{4,\text{hyd}}$ and $\text{RE}_{\text{all}}\text{PO}_{4,\text{hyd}}$ display the same ring pattern as that of the rhabdophane structure. Although the SAED patterns of other $\text{REPO}_{4,\text{hyd}}$ are indistinct due to the large amorphous fractions, the $\text{RE}_i\text{PO}_{4,\text{hyd}}$ ($\text{RE} = \text{Tb-Lu}$) structure can be distinguished from the rhabdophane structure by the lack of an innermost diffraction ring. In EDS analyses, most analytical points from the $\text{RE}_{\text{all}}\text{PO}_4$ crystals contain uniform collective peaks at 4–8 keV corresponding to the L lines of REEs (Figure 10a). However, a few points display non-uniform spectrums, as shown in Figure 10b,c, in which enhanced peaks for Er and Nd occur, respectively.

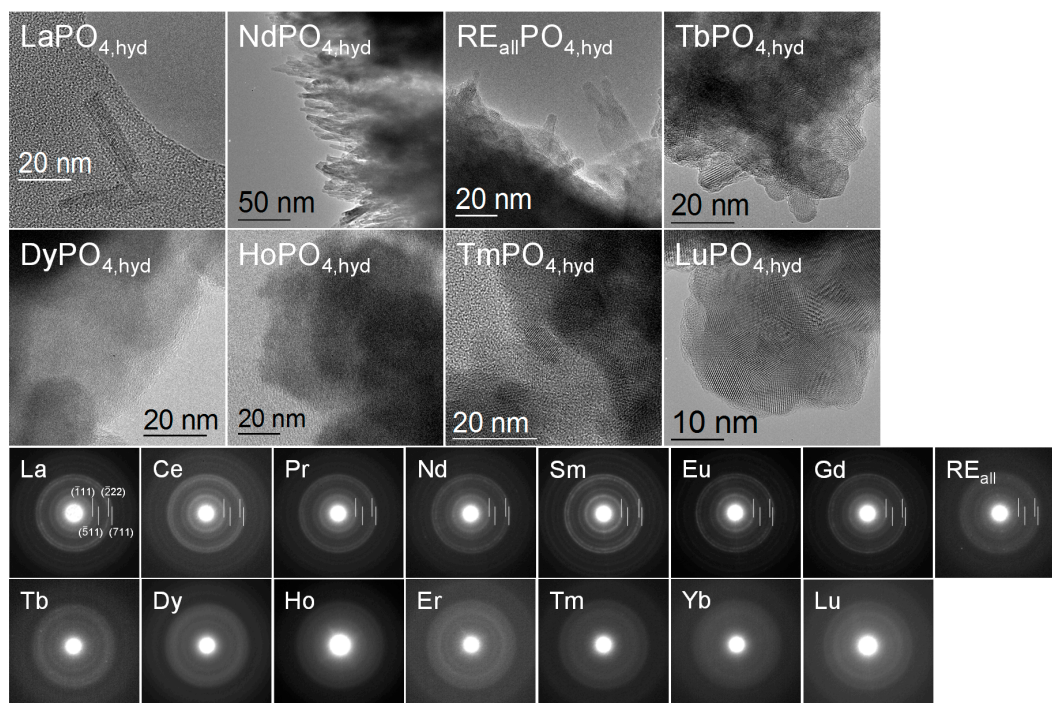


Figure 9. Top panels: Bright-field TEM image of $\text{RE}_i\text{PO}_{4,\text{hyd}}$ ($\text{RE} = \text{La}, \text{Nd}, \text{Tb}, \text{Dy}, \text{Ho}, \text{Tm}, \text{Lu}$) and $\text{RE}_{\text{all}}\text{PO}_{4,\text{hyd}}$ formed at pH 3 for 3 days. Bottom panels: Selected-area electron diffraction pattern of $\text{RE}_i\text{PO}_{4,\text{hyd}}$ ($\text{RE} = \text{La-Lu}$) and $\text{RE}_{\text{all}}\text{PO}_{4,\text{hyd}}$ formed at pH 3 for 3 days. White lines with mirror indices are shown for rhabdophane structure.

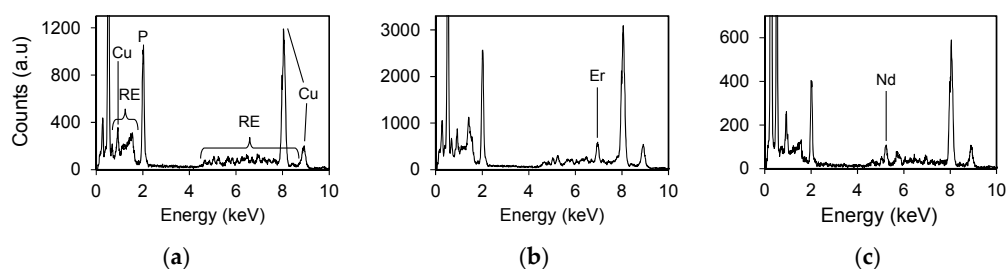


Figure 10. STEM-EDX spectra of $\text{RE}_{\text{all}}\text{PO}_{4,\text{hyd}}$ at (a) a typical point; (b) an Er-rich point; (c) a Nd-rich point. The Cu peak originates from the Cu TEM grid.

$\text{RE}_i\text{PO}_{4,\text{hyd}}$ ($\text{RE} = \text{La}, \text{Tb}, \text{and Yb}$) and $\text{RE}_{\text{all}}\text{PO}_{4,\text{hyd}}$ formed on HAP crystals appear to differ slightly from those formed in mixed solutions. For example, LaPO_4 precipitated as fibrous crystals on HAP (Figure 11a–c), in contrast to the rod-shaped crystals precipitated from the mixed solutions. $\text{RE}_{\text{all}}\text{PO}_{4,\text{hyd}}$ precipitates that formed on HAP exhibit shorter fibrous shaped crystals than the $\text{LaPO}_{4,\text{hyd}}$ precipitates on HAP (Figure 11d–i). The crystal shapes were not significantly affected by the reaction time. $\text{YbPO}_{4,\text{hyd}}$ precipitated at the rim of HAP crystals with a non-fibrous morphology (Figure 11j–k), reflecting the rapid precipitation of $\text{YbPO}_{4,\text{hyd}}$ and consumption of phosphate upon the release of P from the surface of HAP crystals.

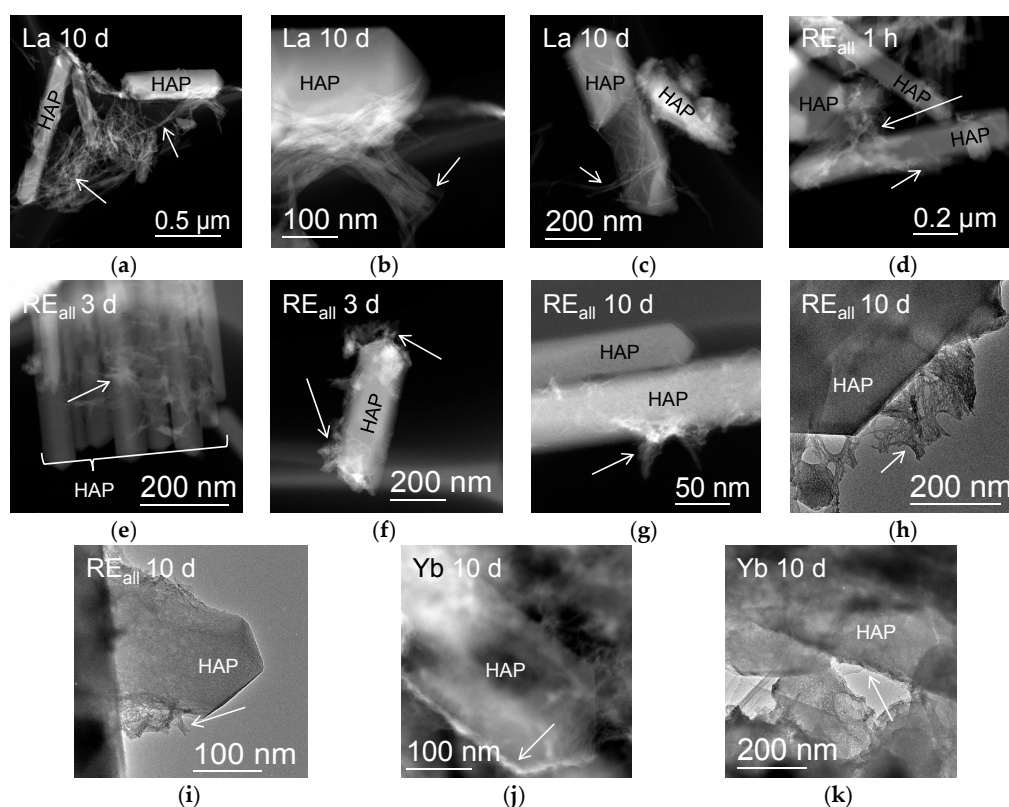


Figure 11. (a–c) HAADF-STEM images of $\text{LaPO}_{4,\text{hyd}}$ during HAP dissolution in contact with a La solution for 10 days. The fibrous nano-crystals indicated by the arrows correspond to $\text{LaPO}_{4,\text{hyd}}$ precipitation. (d) HAADF-STEM image of $\text{RE}_{\text{all}}\text{PO}_{4,\text{hyd}}$ formed during HAP dissolution after 1 h; (e,f) 3 days; (g) 10 days. (h,i) Bright-Field TEM images of the reaction products in all REE solutions after 10 days. The shorter fibrous nano-crystals indicated by the arrows correspond to $\text{RE}_{\text{all}}\text{PO}_{4,\text{hyd}}$ precipitation. (j,k) HAADF-STEM images of $\text{YbPO}_{4,\text{hyd}}$ precipitated on HAP during HAP dissolution in contact with a Yb^{3+} solution for 10 days. $\text{YbPO}_{4,\text{hyd}}$ nano-particles occur at the rim of HAP.

4. Discussion

4.1. Properties of $REPO_{4,hyd}$ Formed at Room Temperature

The $REPO_{4,hyd}$ that formed at room temperature in this study and its characteristics are summarized schematically in Figure 12. The $LREPO_{4,hyd}$ that formed at room temperature exhibited a rhabdophane structure similar to [40]. In this study, monazite did not form a primary product from solution at room temperature, although Hikichi and Hukuo [41] and Hikichi et al. [14] reported that monazite formed from aqueous solutions at 50 °C and pH < 1 within 28 days and at pH 5 after 900 days. Previous studies also reported that monazite was formed at 90 °C from solutions at pH < 1 [40,42], proceeded by the rhabdophane structure losing hydrated waters as a function of the aging time [40]. The differences in pH and the elevated temperatures may account for the absence of monazite in the present experiments at room temperature. This study considers mildly-acidic pH ranges relevant to natural environments without forming RE hydroxides, and the results show that monazite is not likely to form at room-temperature conditions.

Hikichi et al. [14] reported that a churchite structure in $DyPO_4$, YPO_4 , and $YbPO_4$ formed at a pH of 3 at 20 °C; however, Hikichi et al. [43] did not identify a churchite structure for YPO_4 at a pH of 3.7 at 50 °C. The present study also did not detect a churchite structure at a pH of 3 at room temperature. The $HREPO_{4,hyd}$ structure did not match the structure of any RE phosphate minerals, and only a few peaks in the XRD pattern corresponding to the anhydrous tetragonal structure of the xenotime structure appeared in the $HREPO_{4,hyd}$ patterns. Such characteristics in the XRD pattern were also recognized in a previous study by Lucas et al. [40] reporting the synthesis of $YPO_4 \cdot nH_2O$ at 50 °C. As described in the results section, the structure of these phases cannot be identified conclusively. However, it is clear that the $HREPO_{4,hyd}$ structure involves not only amorphous features but also some periodic features. In addition, the structural periodicity is very limited, most likely less than 10 nm as a first approximation based on the XRD peak broadness. Indeed, HRTEM images revealed aggregates of particles as small as ~10 nm. In some cases, although the structure could not be clearly seen initially, electron-beam irradiation resulted in the formation of xenotime structure (Figure 9). Such transformation prevented the acquisition of HRTEM images of $HREPO_{4,hyd}$ particles with their original structure. The evidence implies that the original structure is closely related to very small, nanometer-sized particles with a tetragonal structure similar to that of xenotime.

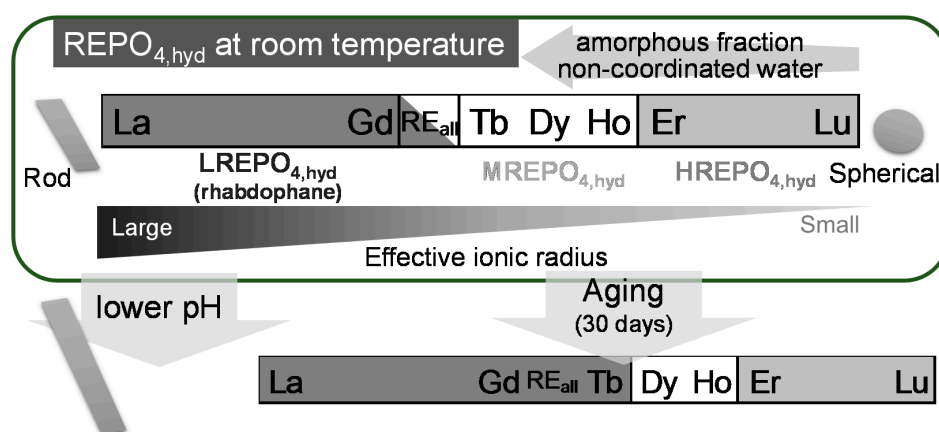


Figure 12. Schematic illustration summarizing the properties of initially formed hydrated RE phosphates.

The presence of a structured component in $HREPO_{4,hyd}$ is also supported by the gradual decrease in wavenumber for band 4, corresponding to the antisymmetric stretching vibration, as a function of the REE ionic radius in the FT-IR spectrum. This feature indicates lattice contraction of a configured structure (Figure 5b). There is evidence that the lattices of monazite, rhabdophane, xenotime, and

churchite contract and appear as a shift in the bands derived from the P–O stretching vibration mode [34,36,44,45]. The lattice shrinks as it incorporates smaller REEs, and the P–O distance becomes slightly shorter, resulting in greater wavenumbers for this vibration. It is noted that HREPO_{4,hyd} is partially composed of amorphous matter in addition to material with a configured structure, as shown in Figure 3b, and only the structured portion contributes to the shift in the wavenumber. The fact that there was no correlation between the effective ionic radius and the antisymmetric stretching vibration wavenumber in the MREPO_{4,hyd} sample may indicate that no configured structure is present in MREPO_{4,hyd}. Although Lucas et al. [40] detected a structural transformation to churchite after 1 h of reaction at 50 °C in solution, no such structural transition was observed in the present study in aging experiments for HREPO_{4,hyd} at room temperature. This indicates that the HREPO_{4,hyd} structure is stable at room temperature and that structural transformation is slow on the time-scale of the present study.

The XRD analysis revealed that the structure of RE_{all}PO_{4,hyd} comprises a combination of the GdPO_{4,hyd} and TbPO_{4,hyd} structures (Figure 1b); however, the both structures in RE_{all}PO_{4,hyd} are not composed of the end member compositions of GdPO_{4,hyd} and TbPO_{4,hyd}. Rather they are composed of all REE at almost same composition as that in the starting reagents as evidenced by the EDX analysis (Figure 10a).

In the LaPO_{4,hyd} precipitation experiments, the crystallite size increased with increasing reaction time from 3 days to 30 days (Figure 1a,d and Figure 2a). This ripening behavior in crystallites was also seen for other REEs, as evidenced by the smaller full-width at half-maximum of diffraction peaks after aging (Figure 1a,d). The crystallite size also increased as pH decreased (Figure 1a,c and Figure 2b). This can be explained by the saturation ratio Ω :

$$\Omega = \left(\frac{IAP_0}{K_{s0}} \right)^{\frac{1}{\eta}} \quad (2)$$

where IAP_0 , K_{s0} , and η refer to the ion activity product ($\text{mol}^2 \cdot \text{dm}^{-6}$), the solubility product ($\text{mol}^2 \cdot \text{dm}^{-6}$), and the number of ions per formula unit, respectively [46]. Using the parameters $K_{s0} = 10^{-25.7}$ [47] and $\eta = 2$ for LaPO₄, the value of Ω at pH 1 was calculated in the present study to be four orders of magnitude smaller than that at pH 5 due to the smaller amount of PO₄³⁻ (Table 7). Stumm [46] recorded that Ω values greater than 1 exponentially induce faster formation of smaller nuclei; hence, lower pH produces larger crystal sizes.

Table 7. Saturation ratio, Ω of the reacting solution with respect to LaPO_{4,hyd}. Activities of RE³⁺ and PO₄³⁻ were calculated using Geochemist’s Workbench with the thermodynamic database *minteq*. The input data are 0.05 mM RE³⁺, 0.05 mM PO₄³⁻, 0.1 M Na⁺, and 0.5 M NO₃⁻.

| pH | Activity ($\text{mol} \cdot \text{dm}^{-3}$) | | Ion Activity Product IAP_0 | Saturation Ratio Ω |
|----|--|------------------------|------------------------------|---------------------------|
| | $a_{\text{RE}^{3+}}$ | $a_{\text{PO}_4^{3-}}$ | | |
| 1 | 2.06×10^{-3} | 8.80×10^{-21} | 1.81×10^{-23} | 3.01×10^1 |
| 3 | 1.29×10^{-3} | 4.95×10^{-16} | 6.37×10^{-19} | 5.65×10^3 |
| 5 | 1.26×10^{-3} | 5.16×10^{-12} | 6.53×10^{-15} | 5.72×10^5 |

4.2. Thermal Stability of RE Phosphates Formed at Room Temperature

Because secondary RE phosphate minerals that form during rock weathering in surface environments are frequently subjected to subsequent thermal events, the thermal stability of REPO_{4,hyd} that formed at room temperature was evaluated. In the present study, the structures of REPO_{4,hyd} were classified into three categories: LREPO_{4,hyd} corresponds to the rhabdophane structure, whereas the structures of both MREPO_{4,hyd} and HREPO_{4,hyd} could not be conclusively identified. The thermal stability of rhabdophane has been thoroughly investigated in previous studies and the rhabdophane

structure is known to be stable up to ~ 500 °C– 800 °C [15,48,49], ~ 750 °C [50]. The present study focused on the thermal stability of the unidentified structures, $\text{MREPO}_{4,\text{hyd}}$ and $\text{HREPO}_{4,\text{hyd}}$, which were stable in air up to 100 – 300 °C on the time-scale of the experiments. The thermal stability of these two types of phosphates was comparable to the stability of $\text{YPO}_4 \cdot 2\text{H}_2\text{O}$, in which the churchite structure transforms to the xenotime structure by annealing at ~ 100 °C for 73 h and at ~ 200 °C within 1 h [50,51]. Non-coordinated water seems to be unrelated to the crystal structure, based on a comparison between the TG-DTA charts and the XRD patterns of heated samples (Figures 4 and 6). Although Mesbah et al. [52] reported that two-step dehydration processes of well-crystalline rhabdophane in detail, the present study demonstrated that structural transitions occurred during the second dehydration step (after the local minimum in the DTG spectrum) for $\text{LREPO}_{4,\text{hyd}}$ and $\text{HREPO}_{4,\text{hyd}}$, or during crystallization (at the DTA peak of exothermic) for $\text{MREPO}_{4,\text{hyd}}$ and $\text{RE}_{\text{all}}\text{PO}_{4,\text{hyd}}$. As noted above, the initial structure can survive up to a certain temperature, at least 120 °C. The $\text{TbPO}_{4,\text{hyd}}$ structure does not possess a perfect rhabdophane structure, but persists up to 300 °C under dry conditions, although rhabdophane forms after 30 days of aging in solution (Figure 1d). Thus, $\text{REPO}_{4,\text{hyd}}$ formed at room temperature is more stable under dry conditions than wet conditions. Therefore, when the average ionic radii are larger than that of Tb (1.04 Å), the initial structure of $\text{REPO}_{4,\text{hyd}}$ is not stable and will transform to the rhabdophane structure by aging under wet conditions at room temperature.

4.3. Formation of $\text{REPO}_{4,\text{hyd}}$ on Apatite at Room Temperature

In $\text{REPO}_{4,\text{hyd}}$ formation experiments using apatite as a source of P, the dissolution rate of HAP in a RE^{3+} solution was determined to be 7.3×10^{-9} mol·m⁻²·min⁻¹ based on the rate of Ca release from HAP for a period of 3–24 h, as shown in Figure 8a. The pH of the solution remained within 5.5–5.6 during the period, after an initial increase in pH from ~ 5.1 in the first 3 h. The dissolution rate calculated in the present study is comparable with the dissolution rate determined by a previous study in pure water; 10^{-7} – 10^{-9} mol·m⁻²·min⁻¹ at pHs ranging from 2–7 [53], indicating that the presence of soluble REEs in solution does not significantly affect the dissolution rate of HAP.

The solution pH adjacent to the HAP surface could be slightly higher than that of the bulk solution. However, RE hydroxide was not characterized in the present study, indicating that the local pH at the HAP surface did not exceed 8.

RE phosphates precipitated at the surface of apatite crystals through dissolution–precipitation mechanisms without the involvement of further mechanisms, such as epitaxial growth and pseudomorphism, which were previously reported in experiments on apatite interaction with aqueous Pb [30]. In general, epitaxial growth and pseudomorphism only occur when the crystallographic characteristics, such as the lattice parameter of the secondary precipitate, are closely related to those of the substrate and when a difference in solubility between the original and secondary mineral acts as the driving force [54–56]. The crystallographic parameters of the RE phosphate precipitates that were characterized in the present study ($\text{LREPO}_{4,\text{hyd}}$ (rhabdophane), $\text{MREPO}_{4,\text{hyd}}$, and $\text{HREPO}_{4,\text{hyd}}$) are not related to those of HAP, preventing the occurrence of those two specific mechanisms. Thus, dissolution–precipitation on apatite surfaces without the lattice relationship is the only mechanism expected for the initial formation of hydrous RE phosphates at ambient temperature in nature. Indeed, rhabdophane crystals associated with apatite were found to be crystallographically unrelated to apatite in natural environments [23], whereas the dissolution–precipitation mechanisms at high temperature >300 °C were reported to exhibit the topotaxial lattice relationship between apatite and monazite [57,58].

5. Implications

In the present study, only the rhabdophane structure was conclusively identified, which was constrained by the average ionic radius calculated according to the proportion of each constituent REE. This finding can be applied to predict the initial structure of hydrated RE phosphates formed in natural

surface environments. However, natural systems involve more complicated species, such as other ions and organic matter. Organic ligands can produce smaller particles [59]. Organic matter, in particular, has the potential to control the stability of the rhabdophane structure, as some previous studies have reported that the rhabdophane structure was stable even for HREE (Yb, Lu) when organic matter was added to the starting reagent [60–62] or mechanical treatment was used to introduce it to the churchite structure [49,63]. A natural occurrence of rhabdophane-Y was reported by Takai and Uehara [64]; however, the mineral they discovered contains a wide variety of other LREE including ~20 wt % La_2O_3 and 15 wt % Nd_2O_3 in addition to ~15 wt % Y_2O_3 . Thus, their report is consistent with the results obtained in the present experiments, which conclude that the structure is determined by the average ionic radius for phases that include multiple REEs.

Aqueous REEs frequently become immobilized in phosphate minerals by the consumption of apatite or they are simply bound to aqueous P during alteration processes [27,64]. Under typical environmental conditions, the hydrated RE phosphates observed in the present study are expected to initially form at nanoscale sizes. As natural water is not supersaturated with regard to RE phosphates [65] when compared with the composition of solutions used in this study, actual RE phosphates may slowly precipitate as larger crystals locally near apatite grains in natural aquifers than those observed in the present study.

The observed development of REE patterns during the formation and aging of $\text{RE}_{\text{all}}\text{PO}_{4,\text{hyd}}$ suggests that REE fractionation during the formation of nanoscale $\text{RE}_{\text{all}}\text{PO}_{4,\text{hyd}}$ is plausible. Therefore, the REE pattern for rhabdophane is not identical to that of the reacting solution. This is of particular importance when mineral REE patterns are used to estimate certain geochemical conditions of the ambient environment, such as oxidation states, compared with REE patterns of bedrock [22]. If specific phosphate minerals such as rhabdophane are dominant in a weathering profile, the chemical composition of the RE phosphate may constrain the bulk REE composition of the weathered profile, as demonstrated by a previous field study [66]. In the present study, only REE fractionation into the rhabdophane structure was examined. Further experiments are needed in order to evaluate REE fractionation into other structures such as $\text{MREPO}_{4,\text{hyd}}$ and $\text{HREPO}_{4,\text{hyd}}$ by varying the average ionic radius over all REEs.

Previous studies highlighted the importance of biomineralization of RE phosphates in constraining the mobility of REEs in the environment [20,21,67]. In these studies, biogenic Ce phosphate was characterized as having a needle-shaped rhabdophane structure [20], while Yb phosphate precipitated as amorphous nanoparticles ~50 nm in size [21]. The structure and morphology of these phases are very similar to those of $\text{LREPO}_{4,\text{hyd}}$ and $\text{HREPO}_{4,\text{hyd}}$ observed in the present study. Hydrous RE phosphate precipitation as a result of microbial activity was also reported in a weathering profile of granite [67]. Given that the majority of P in extracellular substances occurs as orthophosphate [68], the crystallographic nature of biogenic RE phosphates may be mainly controlled by the combined effects of the inorganic reaction processes elucidated in the present study and the effects of organically-bound P species.

Supplementary Materials: The following are available online at www.mdpi.com/2075-163X/7/5/84/s1, Figure S1: XRD patterns of $\text{RE}_i\text{PO}_{4,\text{hyd}}$ (RE = (a) La, (b) Tb, (c) Yb) and (d) $\text{RE}_{\text{all}}\text{PO}_{4,\text{hyd}}$ formed on HAP, Figure S2: Results of deconvolution of the XRD pattern obtained for $\text{REPO}_{4,\text{hyd}}$.

Acknowledgments: This study is partially supported by Japan Science and Technology Agency (JST) Initiatives for Atomic Energy Basic and Generic Strategic Research and by a Grant-in-Aid for Scientific Research (KAKENHI) from the Japan Society for the Promotion of Science (16K12585, 16H04634). The authors would like to thank the emeritus professor, Takashi Murakami, of the University of Tokyo for his detailed comments on the early version of this manuscript, and Hiroyuki Shiotsu for helpful discussions during the course of this study. The authors are grateful to Midori Watanabe for her assistance on XRD, TG-DTA, and FT-IR analyses at the Center of Advanced Instrumental Analysis, Kyushu University. The findings and conclusions of the authors of this paper do not necessarily state or reflect those of the JST.

Author Contributions: Satoshi Utsunomiya conceived and designed the experiments; Asumi Ochiai performed the experiments and analyzed the data; and Asumi Ochiai and Satoshi Utsunomiya wrote the paper.

Conflicts of Interest: The authors declare no conflict of interest.

References

1. Gai, S.; Li, C.; Yang, P.; Lin, J. Recent progress in rare earth micro/nanocrystals: Soft chemical synthesis, luminescent properties, and biomedical applications. *Chem. Rev.* **2014**, *114*, 2343–2389. [[CrossRef](#)] [[PubMed](#)]
2. Chapman, N.A.; Smellie, J.A.T. Special issue—Natural analogs to the conditions around a final repository for high-level radioactive-waste—Introduction and summary of the workshop. *Chem. Geol.* **1986**, *55*, 167–173. [[CrossRef](#)]
3. Choppin, G.R. Comparison of the solution chemistry of the actinides and lanthanides. *J. Less Common Met.* **1983**, *93*, 323–330. [[CrossRef](#)]
4. Choppin, G.R. Comparative solution chemistry of the 4f and 5f elements. *J. Alloys Compd.* **1995**, *223*, 174–179. [[CrossRef](#)]
5. Ni, Y.; Hughes, J.M.; Mariano, A.N. Crystal chemistry of the monazite and xenotime structures. *Am. Mineral.* **1995**, *80*, 21–26. [[CrossRef](#)]
6. Mooney, R.C.L. X-ray diffraction study of cerous phosphate and related crystals. I. Hexagonal modification. *Acta Crystallogr.* **1950**, *3*, 337–340. [[CrossRef](#)]
7. Kohlmann, M.; Sowa, H.; Reithmayer, K.; Schulz, H. Structure of a $Y_{1-x}(Gd,Dy,Er)_xPO_4 \cdot 2H_2O$ microcrystal using synchrotron radiation. *Acta Crystallogr. C* **1994**, *50*, 1651–1652. [[CrossRef](#)]
8. Mesbah, A.; Clavier, N.; Elkaim, E.; Gausse, C.; Kacem, I.B.; Szenknect, S.; Dacheux, N. Monoclinic form of the rhabdophane compounds: $REEPO_4 \cdot 0.667H_2O$. *Cryst. Growth Des.* **2014**, *14*, 5090–5098. [[CrossRef](#)]
9. Braun, J.-J.; Pagel, M.; Herbillon, A.; Rosin, C. Mobilization and redistribution of REEs and thorium in a syenitic lateritic profile: A mass balance study. *Geochim. Cosmochim. Acta* **1993**, *57*, 4419–4434. [[CrossRef](#)]
10. Braun, J.-J.; Viers, J.; Dupré, B.; Polve, M.; Ndam, J.; Muller, J.-P. Solid/liquid REE fractionation in the lateritic system of Goyoum, East Cameroon: The implication for the present dynamics of the soil covers of the humid tropical regions. *Geochim. Cosmochim. Acta* **1998**, *62*, 273–299. [[CrossRef](#)]
11. Stille, P.; Pierret, M.-C.; Steinmann, M.; Chabaux, F.; Boutin, R.; Aubert, D.; Pourcelot, L.; Morvan, G. Impact of atmospheric deposition, biogeochemical cycling and water-mineral interaction on REE fractionation in acidic surface soils and soil water (the Strengbach case). *Chem. Geol.* **2009**, *264*, 173–186. [[CrossRef](#)]
12. Sanematsu, K.; Kon, Y.; Imai, A.; Watanabe, K.; Watanabe, Y. Geochemical and mineralogical characteristics of ion-adsorption type REE mineralization in Phuket, Thailand. *Miner. Depos.* **2013**, *48*, 437–451. [[CrossRef](#)]
13. Berger, A.; Janots, E.; Gnos, E.; Frei, R.; Bernier, F. Rare earth element mineralogy and geochemistry in a laterite profile from Madagascar. *Appl. Geochem.* **2014**, *41*, 218–228. [[CrossRef](#)]
14. Hikichi, Y.; Hukuo, K.; Shiokawa, J. Synthesis of rare earth orthophosphates. *Bull. Chem. Soc. Jpn.* **1978**, *51*, 3645–3646. [[CrossRef](#)]
15. Hikichi, Y.; Murayama, K.; Ohsato, H.; Nomura, T. Thermal changes of rare earth phosphate minerals. *J. Mineral. Soc. Jpn.* **1989**, *19*, 117–126. [[CrossRef](#)]
16. Fang, Y.P.; Xu, A.W.; Song, R.Q.; Zhang, H.X.; You, L.P.; Yu, J.C.; Liu, H.Q. Systematic synthesis and characterization of single-crystal lanthanide orthophosphate nanowires. *J. Am. Chem. Soc.* **2003**, *125*, 16025–16034. [[CrossRef](#)] [[PubMed](#)]
17. Dacheux, N.; Clavier, N.; Podor, R. Monazite as promising long-term radioactive waste matrix: Benefits of high-structural flexibility and chemical durability. *Am. Mineral.* **2013**, *98*, 833–847. [[CrossRef](#)]
18. Deschanel, X.; Seydoux-Guillaume, A.M.; Magnin, V.; Mesbah, A.; Tribet, M.; Moloney, M.P.; Serruys, Y.; Peugeot, S. Swelling induced by alpha decay in monazite and zirconolite ceramics: A XRD and TEM comparative study. *J. Nucl. Mater.* **2014**, *448*, 184–194. [[CrossRef](#)]
19. Yan, R.; Sun, X.; Wang, X.; Peng, Q.; Li, Y. Crystal structures, anisotropic growth, and optical properties: Controlled synthesis of Lanthanide orthophosphate one-dimensional nanomaterials. *Chem. Eur. J.* **2005**, *11*, 2183–2195. [[CrossRef](#)] [[PubMed](#)]
20. Jiang, M.; Ohnuki, T.; Kozai, N.; Tanaka, K.; Suzuki, Y.; Sakamoto, F.; Kamiishi, E.; Utsunomiya, S. Biological nano-mineralization of Ce phosphate by *Saccharomyces cerevisiae*. *Chem. Geol.* **2010**, *277*, 61–69. [[CrossRef](#)]
21. Jiang, M.; Ohnuki, T.; Tanaka, K.; Kozai, N.; Kamiishi, E.; Utsunomiya, S. Post-adsorption process of Yb phosphate nano-particle formation by *Saccharomyces cerevisiae*. *Geochim. Cosmochim. Acta* **2012**, *93*, 30–46. [[CrossRef](#)]

22. Murakami, T.; Utsunomiya, S.; Imazu, Y.; Prasad, N. Direct evidence of late Archean to early Proterozoic anoxic atmosphere from a product of 2.5 Ga old weathering. *Earth Planet. Sci. Lett.* **2001**, *184*, 523–528. [[CrossRef](#)]
23. Ichimura, K.; Murakami, T. Formation of rare earth phosphate minerals in 2.45-Ga paleosol. *J. Mineral. Petrol. Sci.* **2009**, *104*, 86–91. [[CrossRef](#)]
24. Forster, H.J. The chemical composition of REE-Y-Th-U-rich accessory minerals in peraluminous granites of the Erzgebirge-Fichtelgebirge region, Germany. Part II: Xenotime. *Am. Mineral.* **1998**, *83*, 1302–1315. [[CrossRef](#)]
25. Bingen, B.; Demaiffe, D.; Hertogen, J. Redistribution of rare earth elements, thorium, and uranium over accessory minerals in the course of amphibolite to granulite facies metamorphism: The role of apatite and monazite in orthogneisses from southwestern Norway. *Geochim. Cosmochim. Acta* **1996**, *60*, 1341–1354. [[CrossRef](#)]
26. Ohnuki, T.; Kozai, N.; Samadfam, M.; Yasuda, R.; Kamiya, T.; Sakai, T.; Murakami, T. Analysis of uranium distribution in rocks by μ -PIXE. *Nucl. Inst. Methods Phys. Res. B* **2001**, *181*, 586–592. [[CrossRef](#)]
27. Stille, P.; Gauthier-Lafaye, F.; Jensen, K.A.; Salah, S.; Bracke, G.; Ewing, R.C.; Louvat, D.; Million, D. REE mobility in groundwater proximate to the natural fission reactor at Bangombé (Gabon). *Chem. Geol.* **2003**, *198*, 289–304. [[CrossRef](#)]
28. Horie, K.; Hidaka, H.; Gauthier-Lafaye, F. Isotopic evidence for trapped fissionogenic REE and nucleogenic Pu in apatite and Pb evolution at the Oklo natural reactor. *Geochim. Cosmochim. Acta* **2004**, *68*, 115–125. [[CrossRef](#)]
29. Hidaka, H.; Kikuchi, M. SHRIMP in situ isotopic analyses of REE, Pb and U in micro-minerals bearing fission products in the Oklo and Bangombe natural reactors: A review of a natural analogue study for the migration of fission products. *Precamb. Res.* **2010**, *183*, 158–165. [[CrossRef](#)]
30. Kamiishi, E.; Utsunomiya, S. Nano-scale reaction processes at the interface between apatite and aqueous lead. *Chem. Geol.* **2013**, *340*, 121–130. [[CrossRef](#)]
31. Utsunomiya, S.; Ewing, R.C. Application of high-angle annular dark field scanning transmission electron microscopy, scanning transmission electron microscopy-energy dispersive X-ray spectrometry, and energy-filtered transmission electron microscopy to the characterization of nanoparticles in the environment. *Environ. Sci. Technol.* **2003**, *37*, 786–791. [[PubMed](#)]
32. Shannon, R.D. Revised effective ionic radii and systematic studies of interatomic distances in halides and chalcogenides. *Acta Crystallogr. A* **1976**, *32*, 751–767. [[CrossRef](#)]
33. Hezel, A.; Ross, S.D. Forbidden transitions in the infra-red spectra of tetrahedral anions—III. Spectra-structure correlations in perchlorates, sulphates and phosphates of the formula MXO_4 . *Spectrochim. Acta* **1966**, *22*, 1949–1961. [[CrossRef](#)]
34. Assaaoudi, H.; Ennaciri, A.; Rulmont, A. Vibrational spectra of hydrated rare earth orthophosphates. *Vib. Spectrosc.* **2001**, *25*, 81–90. [[CrossRef](#)]
35. Heuser, J.; Bukaemskiy, A.A.; Neumeier, S.; Neumann, A.; Bosbach, D. Raman and infrared spectroscopy of monazite-type ceramics used for nuclear waste conditioning. *Prog. Nucl. Energy* **2014**, *72*, 149–155. [[CrossRef](#)]
36. Kijkowska, R.; Cholewka, E.; Duszak, B. X-ray diffraction and Ir-absorption characteristics of lanthanide orthophosphates obtained by crystallization from phosphoric acid solution. *J. Mater. Sci.* **2003**, *38*, 223–228. [[CrossRef](#)]
37. Masuda, A.; Ikeuchi, Y. Lanthanide tetrad effect observed in marine environment. *Geochem. J.* **1979**, *13*, 19–22. [[CrossRef](#)]
38. Lee, J.H.; Byrne, R.H. Examination of comparative rare earth element complexation behavior using linear free-energy relationships. *Geochim. Cosmochim. Acta* **1992**, *56*, 1127–1137. [[CrossRef](#)]
39. Langmuir, D. *Aqueous Environmental Geochemistry*; Prentice-Hall: Upper Saddle River, NJ, USA, 1997; p. 602.
40. Lucas, S.; Champion, E.; Breigiroux, D.; Bernache-Assollant, D.; Audubert, F. Rare earth phosphate powders $RePO_4 \cdot nH_2O$ (Re = La, Ce or Y)—Part I. Synthesis and characterization. *J. Solid State Chem.* **2004**, *177*, 1302–1311. [[CrossRef](#)]
41. Hikichi, Y.; Hukuo, K. Synthesis of monazite in aqueous solution. *Nippon Kagaku Kaishi* **1975**, *8*, 1311–1314. [[CrossRef](#)]
42. Hukuo, K.; Hikichi, Y. Synthesis of hexagonal cerium phosphate from aqueous solution. *Nippon Kagaku Kaishi* **1975**, *4*, 622–626. [[CrossRef](#)]

43. Hikichi, Y.; Hukuo, K.; Shiokawa, J. Synthesis of xenotime (YPO₄) by precipitation from aqueous solution. *Nippon Kagaku Kaishi* **1978**, *2*, 186–189. [[CrossRef](#)]
44. Begun, G.M.; Beall, G.W.; Boatner, L.A.; Gregor, W.J. Raman spectra of the rare earth orthophosphates. *J. Raman Spectrosc.* **1981**, *11*, 273–278. [[CrossRef](#)]
45. Assaaoudi, H.; Ennaciri, A. Vibrational spectra and structure of rare earth orthophosphates, weinschenkite type. *Spectrochim. Acta A* **1997**, *53*, 895–902. [[CrossRef](#)]
46. Stumm, W. *Chemistry of the Solid-Water Interface. Processes at the Mineral-Water and Particle-Water Interface in Natural Systems*; John Wiley & Sons: New York, NY, USA, 1992; p. 428.
47. Cetiner, Z.S.; Wood, S.A.; Gammons, C.H. The aqueous geochemistry of the rare earth elements. Part XIV. The solubility of rare earth element phosphates from 23 to 150 °C. *Chem. Geol.* **2005**, *217*, 147–169. [[CrossRef](#)]
48. Utsunomiya, S.; Murakami, T.; Nakada, M.; Kasama, T. Iron oxidation state of a 2.45-Byr-old paleosol developed on mafic volcanics. *Geochim. Cosmochim. Acta* **2003**, *67*, 213–221. [[CrossRef](#)]
49. Hikichi, Y.; Sasaki, T.; Murayama, K.; Nomura, T. Mechanochemical changes of weinschenkite-type RPO₄·2H₂O (R = Dy, Y, Er, or Yb) by grinding and thermal reactions of the ground specimens. *J. Am. Ceram. Soc.* **1989**, *72*, 1073–1076. [[CrossRef](#)]
50. Lucas, S.; Champion, E.; Bernache-Assollant, D.; Leroy, G. Rare earth phosphate powders RePO₄·nH₂O (Re = La, Ce or Y)—Part II. Thermal behavior. *J. Solid State Chem.* **2004**, *177*, 1312–1320. [[CrossRef](#)]
51. Hikichi, Y.; Hukuo, K.; Shiokawa, J. Synthesis of monoclinic YPO₄·2H₂O and its thermal change. *Nippon Kagaku Kaishi* **1977**, *11*, 1634–1638. [[CrossRef](#)]
52. Mesbah, A.; Clavier, N.; Elkaim, E.; Szenknect, S.; Dacheux, N. In pursuit of the rhabdophane crystal structure: From the hydrated monoclinic LnPO₄·0.667H₂O to the hexagonal LnPO₄ (Ln = Nd, Sm, Gd, Eu and Dy). *J. Solid State Chem.* **2017**, *249*, 221–227. [[CrossRef](#)]
53. Valsami-Jones, E.; Ragnarsdottir, K.V.; Putnis, A.; Bosbach, D.; Kemp, A.J.; Cressey, G. The dissolution of apatite in the presence of aqueous metal cations at pH 2–7. *Chem. Geol.* **1998**, *151*, 215–233. [[CrossRef](#)]
54. Putnis, A. Mineral replacement reactions: from macroscopic observations to microscopic mechanisms. *Mineral. Mag.* **2002**, *66*, 689–708. [[CrossRef](#)]
55. Putnis, A.; Putnis, C.V. The mechanism of reequilibration of solids in the presence of a fluid phase. *J. Solid State Chem.* **2007**, *180*, 1783–1786. [[CrossRef](#)]
56. Xia, F.; Brugger, J.; Chen, G.; Ngothai, Y.; O'Neill, B.; Putnis, A.; Pring, A. Mechanism and kinetics of pseudomorphic mineral replacement reactions: A case study of the replacement of pentlandite by violarite. *Geochim. Cosmochim. Acta* **2009**, *73*, 1945–1969. [[CrossRef](#)]
57. Harlov, D.E.; Wirth, R.; Förster, H.-J. An experimental study of dissolution-reprecipitation in fluorapatite: Fluid infiltration and the formation of monazite. *Contrib. Mineral. Petrol.* **2005**, *150*, 268–286. [[CrossRef](#)]
58. Harlov, D.E. Apatite: A fingerprint for metasomatic processes. *Elements* **2015**, *11*, 171–176. [[CrossRef](#)]
59. Boakye, E.E.; Mogilevsky, P.; Hay, R.S. Synthesis of nanosized spherical rhabdophane particles. *J. Am. Ceram. Soc.* **2005**, *88*, 2740–2746.
60. Hikichi, Y.; Ota, T.; Hattori, T.; Imaeda, T. Synthesis and thermal reactions of rhabdophane-(Y). *Mineral. J.* **1996**, *18*, 87–96. [[CrossRef](#)]
61. Min, W.; Daimon, K.; Ota, T.; Matsubara, T.; Hikichi, Y. Synthesis and thermal reactions of rhabdophane-(Yb or Lu). *Mater. Res. Bull.* **2000**, *35*, 2199–2205. [[CrossRef](#)]
62. Ito, H.; Fujishiro, Y.; Sato, T.; Okuwaki, A. Preparation of lanthanide orthophosphates by homogeneous precipitation under hydrothermal conditions using lanthanide-EDTA chelates. *Br. Ceram. Trans.* **1995**, *94*, 146–150.
63. Hikichi, Y.; Yogi, K.; Ota, T. Preparation of rhabdophane-type RPO₄·nH₂O (R = Y or Er, n = 0.7–0.8) by pot-milling churchite-type RPO₄·2H₂O at 20–25 °C in air. *J. Alloys Compd.* **1995**, *224*, L1–L3. [[CrossRef](#)]
64. Takai, Y.; Uehara, S. Rhabdophane-(Y), YPO₄·H₂O, a new mineral in alkali olivine basalt from Hinodematsu, Genkai-cho, Saga Prefecture, Japan. *J. Mineral. Petrol. Sci.* **2012**, *107*, 110–113. [[CrossRef](#)]
65. Roncal-Herrero, T.; Rodríguez-Blanco, J.D.; Oelkers, E.H.; Benning, L.G. The direct precipitation of rhabdophane (REEPO₄·nH₂O) nano-rods from acidic aqueous solutions at 5–100 °C. *J. Nanopart. Res.* **2011**, *13*, 4049–4062. [[CrossRef](#)]

66. Aubert, D.; Stille, P.; Probst, A. REE fractionation during granite weathering and removal by waters and suspended loads: Sr and Nd isotopic evidence. *Geochim. Cosmochim. Acta* **2001**, *65*, 387–406. [[CrossRef](#)]
67. Taunton, A.E.; Welch, S.A.; Banfield, J.F. Microbial controls on phosphate and lanthanide distributions during granite weathering and soil formation. *Chem. Geol.* **2000**, *169*, 371–382. [[CrossRef](#)]
68. Masaki, S.; Shiotsu, H.; Ohnuki, T.; Sakamoto, F.; Utsunomiya, S. Effects of CeO₂ nanoparticles on microbial metabolism. *Chem. Geol.* **2015**, *391*, 33–41. [[CrossRef](#)]



© 2017 by the authors. Licensee MDPI, Basel, Switzerland. This article is an open access article distributed under the terms and conditions of the Creative Commons Attribution (CC BY) license (<http://creativecommons.org/licenses/by/4.0/>).